

CAP: Commutative Algebra Prediction of Protein-Nucleic Acid Binding Affinities

Mushal Zia¹, Faisal Suwayyid ^{1,2}, Yuta Hozumi* ¹
 JunJie Wee¹, Hongsong Feng³, and Guo-Wei Wei^{†1,4,5}

¹Department of Mathematics,
 Michigan State University, MI 48824, USA.

²Department of Mathematics,
 King Fahd University of Petroleum and Minerals, Dhahran 31261, KSA.

³Department of Mathematics and Statistics,
 University of North Carolina at Charlotte, Charlotte, NC 28223, USA

⁴Department of Electrical and Computer Engineering,
 Michigan State University, MI 48824, USA.

⁵Department of Biochemistry and Molecular Biology,
 Michigan State University, MI 48824, USA.

Abstract

An accurate prediction of protein-nucleic acid binding affinity is vital for deciphering genomic processes, yet existing approaches often struggle in reconciling high accuracy with interpretability and computational efficiency. In this study, we introduce commutative algebra prediction (CAP), which couples persistent Stanley-Reisner theory with advanced sequence embedding for predicting protein-nucleic acid binding affinities. CAP encodes proteins through transformer-learned embeddings that retain long-range evolutionary context and represents DNA and RNA with k -mer algebra embeddings derived from persistent facet ideals, which capture fine-scale nucleotide geometry. We demonstrate that CAP surpasses the SVSBI protein-nucleic acid benchmark and, in a further test, maintains reasonable performance on newly curated protein-RNA and protein-nucleic acid datasets. Leveraging only primary sequences, CAP generalizes to any protein-nucleic acid pair with minimal preprocessing, enabling genome-scale analyses without 3D structural data and promising faster virtual screening for drug discovery and protein engineering.

Keywords: Persistent commutative algebra, facet persistence barcodes, persistent ideals, machine learning, protein-nucleic acid binding.

*Current address: School of Mathematics, Georgia Institute of Technology, Atlanta, GA, USA.

†Corresponding author: Guo-Wei Wei (weig@msu.edu).

Contents

1	Introduction	2
2	Results and Discussion	5
2.1	Overview of the CAP model	5
2.2	Protein-Nucleic Acid Binding Affinity Prediction	5
2.3	Discussion	7
3	Datasets	8
4	Methods	10
4.1	Persistent Stanley-Reisner Theory	10
4.2	1-mer Algebra	11
4.3	Vectorization of persistent comutative algebra	12
4.4	Transformer-based protein language model	12
4.5	Machine learning modeling	13
4.6	Evaluation metrics	13
5	Model interpretability	14
6	Conclusion	15

1 Introduction

Protein-nucleic acid recognition underpins a spectrum of essential biological processes. These processes form the backbone of cellular processes central to life, ranging from DNA replication, transcription, genome stability to RNA transport, splicing, and post-transcriptional regulation. An accurate modeling of protein-DNA and protein-RNA binding is crucial not only for fundamental biology but also for therapeutic innovations, accelerating genomic medicine, synthetic biology, and drug design [1]. Molecular-level mechanisms are mediated by proteins through recognition and binding to specific DNA or RNA sequences. Such mechanisms includes hydrogen bonding, electrostatic attraction, hydrophobic interaction, physicochemical force, and structural complementarity. Disruption in such binding events can lead to the development of various diseases such as, cancer, neurodegenerative conditions, and autoimmune disorders [2]. Thus, the orchestration of these associations is crucial not only for decoding biomolecular functions but also for paving the way to new therapies and drug discovery.

A variety of conventional techniques have been adopted in past for the gold-standard measurement of binding affinity predictions of protein-protein/ligand systems, like fluorescence spectroscopy, electrophoretic mobility shift assays (EMSA), surface plasmon resonance (SPR), isothermal titration calorimetry, and filter binding [3]. However, they are typically resource-intensive and time consuming. To address these limitations, a spectrum of *in silico* strategies have been developed. Classical physics-based methods such as thermodynamic integration, free energy perturbation, molecular Mechanics Poisson-Boltzmann Surface Area (MM-PBSA) offer detailed estimates but are particularly laborious for large biomolecular systems. Non-classical approaches include but not limited to knowledge-driven potentials [4], empirical scoring functions [5], force-field scoring functions [6], and machine-learning approaches using engineered descriptors [7]. These methods have delivered promising results in protein-protein or protein-ligand systems. However, they tend to underperform on DNA owing to its unique conformational complexities and lack of availability of comprehensive binding affinity datasets.

On the other hand, various experimental and computational approaches have been applied over the past decade to understand protein-RNA interactions, ranging from high-throughput CLIP-seq [8], purely seq-based prediction algorithms [9, 10, 11] to knowledge-based scoring [12] and coarse-grained docking [13]. In addition, resolving protein-RNA complex structures through X-ray crystallography or nuclear magnetic resonance (NMR) is hampered by inherent flexibility of many RNA partners which makes such determinations technically challenging and prohibitively slow. Although several protein-RNA docking approaches have substantially accelerated the discovery of RNA-protein interaction sites and expanded available structural decoys, yet none provide quantitative binding affinity measurements, leaving a paucity of RNA affinity data [14].

In light of these limitations, data-driven models, particularly those built on machine-learning (ML) frameworks, have recently reshaped computational molecular biology by emerging as an integral components for modern drug design [15, 16]. The integration of bioinformatics [17] with ML and deep learning, when applied to protein-nucleic acid systems, has demonstrated promising shift by enabling the prediction of molecular interactions in a complex high-dimensional data at an unprecedented scale. Recently, mathematical artificial intelligence (AI), particularly topological deep learning (TDL) first introduced in 2017 [18], has emerged as a new paradigm for rational learning in data science [19], leading to a new frontier for modeling intricate biomolecular systems[20], such as proteins and their interactions [21, 22]. Notably, mathematical AI secured victories in D3R Grand Challenges, an annual worldwide competition series in computer-aided drug design [23, 24].

Recently, topological sequence analysis (TSA) has been proposed as a viable approach for biological sequence modeling [25]. Delta complex approaches of TSA enable the efficient treatment of large genomic sequences [26], while category theory approaches of TSA achieve higher accuracy for nearly identical genetic variants [27].

Some early studies laid important groundwork for protein-DNA binding interactions using ML frameworks, such as Zhao et al.’s atomic pairwise statistical potential (DDNA3) [28], Rastogi et al.’s sequencing-based affinity profiling [29], and Barissi et al.’s physics-based machine-learning method (DNAffinity) [30]. Building on these advances, subsequent models such as PreDBA [31], PDA-Pred [32], and emPDBA [33] have broadened the affinity-prediction toolbox. Likewise, for protein-RNA interactions, Yang et al. [34] assembled the first quantitative dataset of protein-RNA affinities, which was later followed by the development of several structure-driven learning frameworks, each developed with its own curated dataset, including the methods proposed by Nithin et al. [5] and PredPRBA [35], as well as models including Hong et al. [36] and the more recent PRA-Pred [37]. Though these advancements have pushed the field forward, yet most approaches rely on stacked regressors, class-specific framework architectures to curb overfitting in small datasets, and basic interface metrics.

Commutative algebra is a mathematical study of commutative rings, their ideals, modules, and related structures [38]. As a foundational framework in pure mathematical fields such as algebraic number theory, homological algebra, and algebraic geometry, commutative algebra has seen limited application in data science and the biological sciences. In a recent effort, Suwayyid and Wei introduced persistent Stanley-Reisner theory (PSRT) to forge a connection between commutative algebra, algebraic topology, data science, and machine learning [39]. This method has already yielded promising results in protein-ligand binding affinity predictions via a structure-based approach [40].

The Stanley-Reisner theory investigates the commutative algebra of simplicial complexes, assemblies of vertices, edges, triangles, and their higher-order faces, through the study of square-free monomial ideals in polynomial rings [41, 42]. PSRT integrates these notions with multiscale analysis, enabling commutative algebra learning and predictions. PSRT examines the evolution of Stanley-Reisner ideal across a filtration, yielding a range of algebraic and topological invariants, such as persistent graded Betti numbers (computed via Hochster’s formula), persistent f- and h-vectors, and persistent facet ideals. In particular, facet-persistence barcodes which document the “birth” and “death” of each facet ideal during filtration have been developed for real-world data applications. Thus, PSRT is a new multiscale approach that offers rich geometric, topological, and combinatorial analysis not readily accessible to conventional mathematical, statistical, and physical approaches.

In this study, we investigate commutative algebraic predictions (CAPs) for the sequence-based modeling of protein-nucleic acid binding affinities, a direction not previously explored. Our CAP offers algebraic sequence analysis (ASA), an algebra-based sequence-driven alternative to conventional structure-based approaches, facilitating an effective modeling of biomolecular interactions using primary sequence information alone. We employ a dataset assembled by Shen *et al.* [11], comprising 186 protein-nucleic acid complexes derived from the PDBbind v2020 database, referred to here as S186. Each complex in this dataset is represented by pairing rich residue-level embeddings of the protein sequence with nucleotide-level descriptors of the associated nucleic acid strand (DNA or RNA). These complementary sequence-based features implicitly capture interactions such as hydrogen bonding, electrostatic contacts, base stacking, and van der Waals forces. Additionally, we evaluate CAP on two newly curated datasets: a protein-RNA dataset (S142) con-

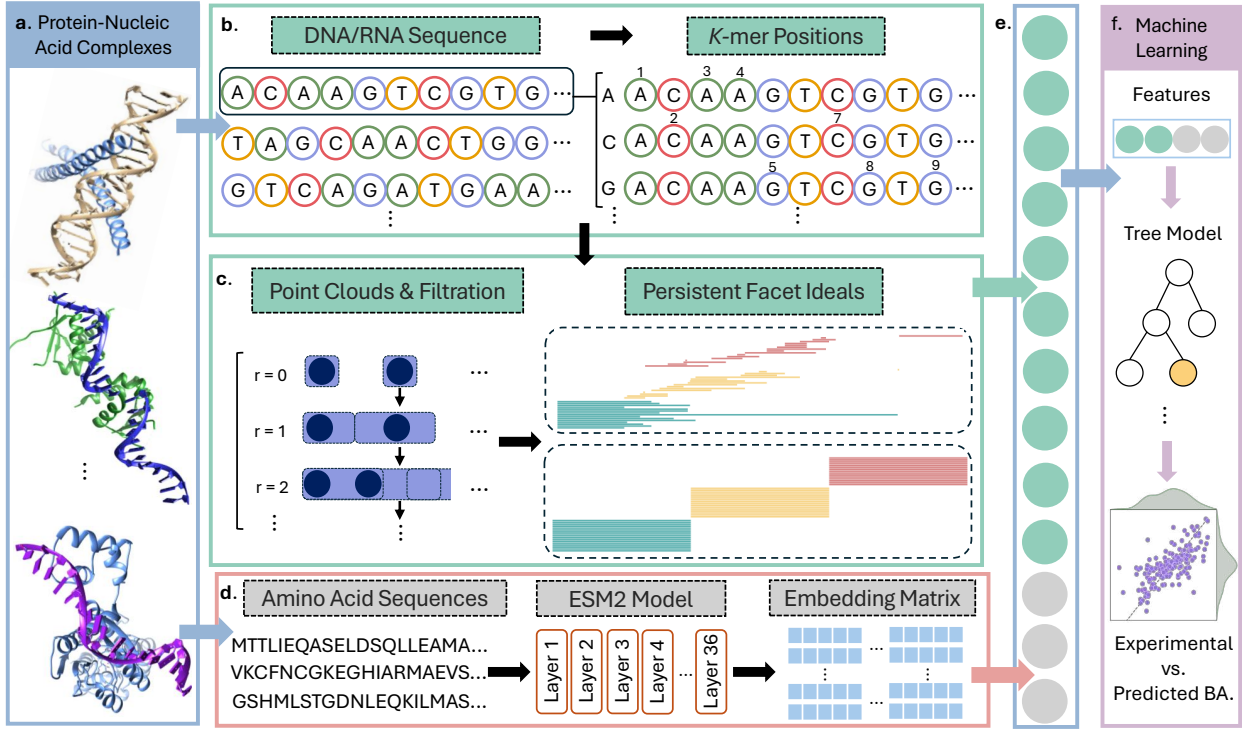


Figure 1: Illustration of the workflow in CAP. (a) Protein-nucleic acid complexes. (b) k -mers are extracted from the DNA sequences of the given complexes. For each k -mer=1, the set of its occurrence positions within the sequence is treated as an input data. (c) The persistent facet ideals associated with these input data for three dimensions are then computed and used as topological features for the corresponding k -mers. (d) From the amino acid sequence for the given complexes, 2560 embedding vectors are generated using state-of-the-art ESM2 model with 36 layers. (e) The feature vectors of all DNA and proteins are concatenated to construct a genome-level topological representation. (f) Finally, our CAP model is trained using these features with machine learning techniques for the prediction task.

taining 142 complexes, and a protein-nucleic acid dataset (S322) containing 322 complexes. The results demonstrate CAP’s robust predictive performance, highlighting a promising new approach for affinity prediction without explicit reliance on structural models.

In the following sections, we present our results followed by a brief discussion on existing methodologies, the two new datasets, and feature extraction processes with a detailed demonstration of robust predictive performance of CAP for protein-nucleic acid binding affinity. We also elaborate on the mathematical foundations and computational interpretability of CAP. Finally, we conclude by discussing our findings and outlining potential future research directions.

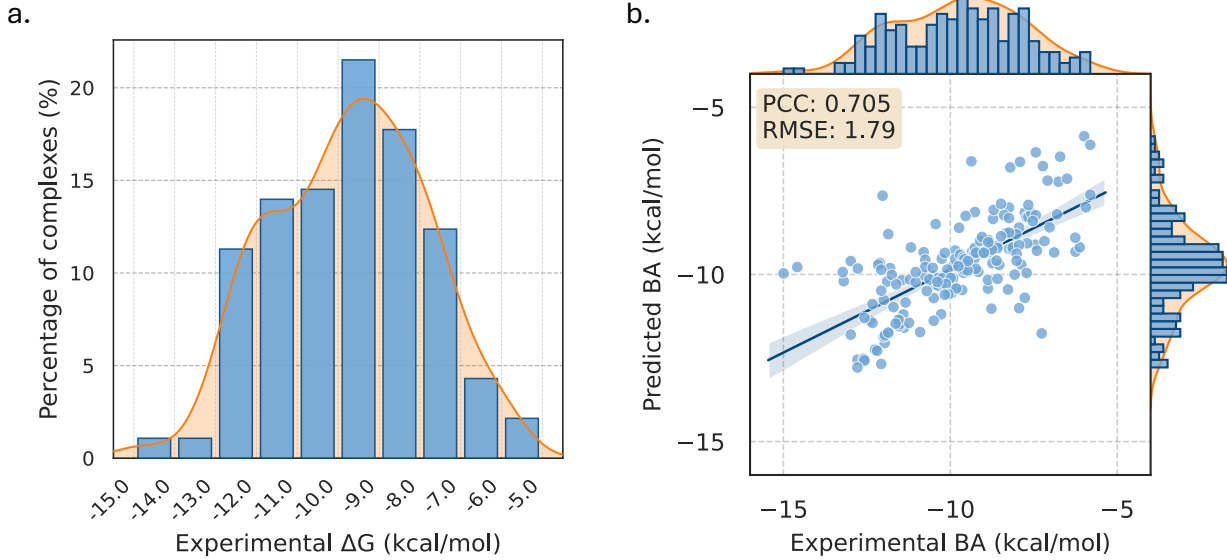


Figure 2: (a) Distribution of experimental binding affinity (ΔG) in the S186 dataset. (b) A comparison between the experimental binding affinities and the predicted values from our CAP model for this dataset. The corresponding Pearson correlation coefficient (PCC) value is 0.705 with an RMSE of 1.79 kcal/mol.

2 Results and Discussion

2.1 Overview of the CAP model

Figure 1 illustrates the workflow of the proposed CAP model. For a given protein-nucleic acid complex (a), the nucleic acid sequence is processed with PSRT (b-c) to provide a CAP feature vector. Meanwhile, the protein sequence is processed with the ESM2 model to result in an embedding matrix (d). The combined feature vector (e) is fed into a machine learning model (f). More details of protein sequence embedding, nucleic acid sequence analysis, and machine learning parametrization can be found in the methods section.

2.2 Protein-Nucleic Acid Binding Affinity Prediction

A vital category of biomolecular interactions involves protein-nucleic acid binding which underpins essential cellular processes such as, catalysis, molecular transport, signal transduction, transcription, and translation. Moreover, these interactions preserves chromosomal integrity and regulates gene expression however, can contribute to pathologies including cancer, genetic disorders, autoimmune diseases. Understanding how hydrogen bonds, van der Waals contacts, dipole-dipole interactions, electrostatics, van der Waals attractions, and hydrophobicity contribute to binding affinities then informs the rational design of new therapeutics such as structure-based drug design. In this study, we apply our CAP framework to capture these interactions and predict protein-nucleic acid binding affinity.

We begin by evaluating the predictive accuracy of our PSRT-guided framework on the S186 dataset

against the SVSBI model on protein-nucleic acid binding affinity [11]. Due to a lack of established benchmarks, Shen *et al.* [11] assembled a dataset of 186 protein-nucleic acid complexes. In order to construct a high-quality dataset from PDBbind-v2020, the authors applied four stringent filters: (i) a complex was retained only if it contained one unique protein sequence and one unique nucleic acid sequence. Furthermore, multiple chains carrying the same sequence were allowed, but any chain with mixed or hybrid bases (e.g., both T and U) was discarded; (ii) only complexes with experimentally determined binding affinities measured at 298 K were kept; (iii) entries containing ambiguous labels (\sim , $<$, or $>$) were not considered; (iv) exclude those complexes that whose nucleic acid sequence length is fewer than 5.

The SVSBI framework leverages an ESM-based Transformer for proteins and DNABERT for nucleic acids and records an average Pearson of 0.669 and RMSE of 1.98 kcal/mol. On the other hand, CAP achieves robust prediction performance with a Pearson correlation coefficient PCC of 0.705 with RMSE of 1.79 kcal/mol, surpassing the existing SVSBI model [11] for the protein-nucleic binding affinity prediction on the same dataset as shown in Table 1. Furthermore, we analyze the distribution of experimental binding affinity ΔG values of S186 as shown in Figure 2a. We also observe that ΔG ranges from -15 kcal/mol to -6 kcal/mol and 66% of the complexes have ΔG of -11 to -7 kcal/mol. An illustrative comparison between the experimental binding affinities and the predicted values from our CAP model for this dataset is presented in Figure 2b and a full comparison of experimental and predicted binding affinities is provided in Table ???. In addition, a representation of how binding free energy varies with sequence length in S186 is represented in Figure 3a. While the strand lengths range from 5 to 45~nt, we observe that the shortest strands (5~nt) bind weakly on average (mean $\Delta G = -7.77$ kcal/mol), whereas the longest strands (45~nt) reach an average $\Delta G = -9.57$ kcal/mol. Moreover, we also note that the length interval with the highest coverage (10-15~nt, 67 complexes) has a mean ΔG of -9.32 kcal/mol. Our CAP framework provides a powerful and structure-free method, even though that the size of our dataset is modest.

Table 1: Comparison of prediction performance between existing SVSBI model and our model, CAP, on S186 for protein-nucleic acid binding affinity prediction. Reported metrics include Pearson correlation coefficient (PCC) and RMSE values in kcal/mol. All results are averaged over twenty independent runs with different random seeds, and the average metric values are reported.

Model	PCC	RMSE (kcal/mol)
SVSBI [11]	0.669	1.98 ¹
CAP	0.705	1.79

Several existing protein-DNA affinity models [28, 31, 32, 33] and protein-RNA models [35, 36, 37] have broadened the binding prediction toolbox. However, they depend on large, handcrafted feature sets and category-specific tuning steps that complicate workflows and have limit generalizability. CAP sidesteps these limitations by coupling persistent Stanley-Reisner theory with a concise sequence-level interaction embedding and a single gradient-boosting regressor. By summarizing residue-nucleotide contacts directly from the paired protein and nucleic-acid sequences, CAP removes the need to count hydrogen bonds, tally base-pair frequencies, model stacking ensembles, or train separate predictors for different structural subclasses. Because CAP relies solely on primary sequences, it can be applied to any protein-DNA/RNA pair without 3D structures, subclass labels, or bespoke feature engineering, offering higher predictive power with far less manual effort and

¹The original RMSE of 1.45 reported by Shen et al. [11] was not converted into kcal/mol; here we apply the factor 1.3633 to obtain 1.98 kcal/mol.

providing an extensible framework for large-scale studies of protein-nucleic recognition.

2.3 Discussion

Within the spectrum of existing binding affinity approaches for protein-DNA, the most recent is emPDBA [33], which integrates 106 sequence- and structure-based features into a stacking ensemble applied to 340 protein-DNA complexes at 40 % protein sequence similarity. After subclassifying DNA by structural form and applying feature selection method, it reaches a correlation value of 0.66 with mean absolute error (MAE) = 1.24 kcal/mol, compared with 0.12 (MAE = 1.64 kcal/mol) on an unclassified set. Another model, PDA-Pred [32], built on 117 features for each of the 391 complexes at 25 % sequence identity, employs similar classifications of DNA structures and with an additional protein functional categorization followed by a feature selection method (jack-knife) to achieve $PCC = 0.78$, dropping to just $PCC = 0.21$ without any categorization. Furthermore, on a common independent testing set of 36 complexes, emPDBA showed an $PCC = 0.53$ with MAE = 1.11 kcal/mol, whereas earlier ensemble regression methods like PreDBA [31] attained $PCC = 0.30$, and the statistical potential DDNA3 [28] only $PCC = 0.09$ with MAE = 2.05 kcal/mol and MAE = 1.80 kcal/mol, respectively.

While numerous models exist for protein-DNA binding affinity prediction, there are only a limited number of models available for predicting protein-RNA binding affinity [35, 36, 37]. The most recent, PRA-Pred model [37], consists of 217 protein-RNA complexes with proteins clustered at a 25% sequence identity cutoff, adopts a classification strategy similar to that used in protein-DNA binding affinity prediction. It categorizes RNA into five structural subclasses and proteins into functional categories and achieves a Pearson correlation of 0.77 and a mean absolute error (MAE) of 1.02 kcal/mol using a jack-knife feature selection strategy. On the standard blind set of 44 complexes, the model obtains an overall performance of $PCC = 0.60$ with an MAE of 1.47 kcal/mol. Another model, PRdeltaGPred [36], starts with 63 interface-based features and applies a custom feature reduction process to improve prediction accuracy. Despite this tailored feature selection strategy, PRdeltaGPred reports $PCC = 0.41$ with an MAE of 1.83 kcal/mol on the standard 44-complex blind set. The third model, PredPRBA [35], is trained on 103 protein-RNA complexes filtered at a 40% sequence identity cutoff. It makes use of both sequence-level and structural features at the whole-complex level, and applies jack-knife test within six predefined RNA subclasses. While the model’s overall performance on the standard 44-complex blind test is limited ($PCC = 0.07$, MAE = 2.07 kcal/mol, its best pre-classification performance reaches $PCC = 0.48$, suggesting that feature and label heterogeneity across RNA types poses a challenge for unified modeling.

Table 2: Prediction performance of CAP on S142 and S322 datasets.

Dataset	PCC	RMSE (kcal/mol)
S142	0.653	2.18
S322	0.669	2.00

These earlier studies on protein-DNA/RNA affinity predictions have reported results on datasets clustered anywhere from strict 25% identity to no clustering at all, making headline metrics hard to compare across papers. In our study, we employ the S186 dataset [11] that solely focus on biochemical uniformity (single protein-nucleic complex per entry, unambiguous labels, identical assay temperature). The resulting dataset, though modest in size, spans a balanced range of

binding energies and local neighborhoods, so model performance is driven by genuine physico-chemical signal rather than by the occasional near-duplicate chain. Encouraged by these stable results and to further assess our CAP framework on protein-RNA binding affinity, we curated the S142 dataset of 142 protein-RNA complexes. On this set, our model achieves a *PCC* of 0.653 and an RMSE of 2.18 kcal/mol; evaluation on an expanded dataset, S322, of 322 protein-nucleic acid complexes yields better performance (*PCC* = 0.669, RMSE = 2.0 kcal/mol). A prediction performance of both datasets can be found in Table 2, whereas a full comparison of experimental and predicted binding affinities for S142 and S322 are presented in Table ?? and Table ??, respectively, along with the corresponding PDBIDs.

Taken together, our CAP framework proposes a more unified approach. It uses a purely sequence-based interaction embedding, built from learned residue and nucleotide descriptors, so it requires neither three-dimensional structures, subclass labels, nor hand-crafted interface features. Furthermore, the existing models in literature run a separate regression model for every DNA/RNA subclass steps that complicate the workflow and risk information loss. Moreover, the datasets used in this study have been carefully curated to include only bona-fide DNA/RNA-binding proteins and complexes containing exactly one protein chain and one DNA/RNA chain. By removing mixed or multifunctional assemblies, the model sees a cleaner and functionally coherent signal with spurious inter-protein contacts that do not contribute to the reported affinity being eliminated.

3 Datasets

In this section, we give a brief insight about the datasets used in this study, the data collection and curation. Dataset S186 is given by Shen *et al.* [11]. It contains mostly protein-DNA complexes but has a few protein-RNA complexes as well. We created a protein-RNA dataset S142 and a protein-nucleic acid dataset S322. Both datasets were assembled by merging our own curated complexes from PDBbind-v2020 with some of the complexes used in the PRA-Pred study [37]. We followed the filtering pipeline of Shen *et al.* [11], with several additional steps to improve consistency and reliability. First, all non-standard bases were removed, retaining only *A*, *C*, *G* and *T* for DNA, and *A*, *C*, *G* and *U* for RNA. Complexes having at least one nucleotide were also kept. Although a subset of the S142 and S322 complexes also appears in other studies (e.g., PRdeltaG-Pred [36] and PredPRBA [35]), all retained entries passed our independent quality checks. Finally, an additional filter applied to the RNA subsets of both datasets removed systems that do not involve bona-fide RNA-binding proteins, ensuring that the remaining complexes represent genuine RBP-RNA interactions rather than incidental co-crystallisations. RNA-binding proteins often belong to well-studied families such as RNA-recognition motifs (RRMs), K-homology (KH) domains, and double-stranded RNA-binding domains (dsRBDs) [43]. These folds rely on recurring chemical strategies: clusters of lysine and arginine neutralise the phosphate backbone, while aromatic side chains stack against exposed bases or the ribose 2'-hydroxyl [43]. Because those interaction chemistries are reused across many RBPs, the overall contact signatures are comparatively uniform. We therefore restrict our RNA dataset to bona-fide RBPs and group complexes by functional class, giving CAP a chemically coherent training set. DNA-binding proteins, in contrast, encompass a broader spectrum of folds including major-groove readers, backbone clamps, and helix-wrapping architectural proteins and thus, display far more heterogeneous residue-nucleotide contact patterns [44]. The same functional filtering sharpens the RNA dataset but is less beneficial for DNA, where preserving the full diversity of recognition modes is essential. Overall, this unified and rigorously filtered dataset collection underpins the evaluation of CAP.

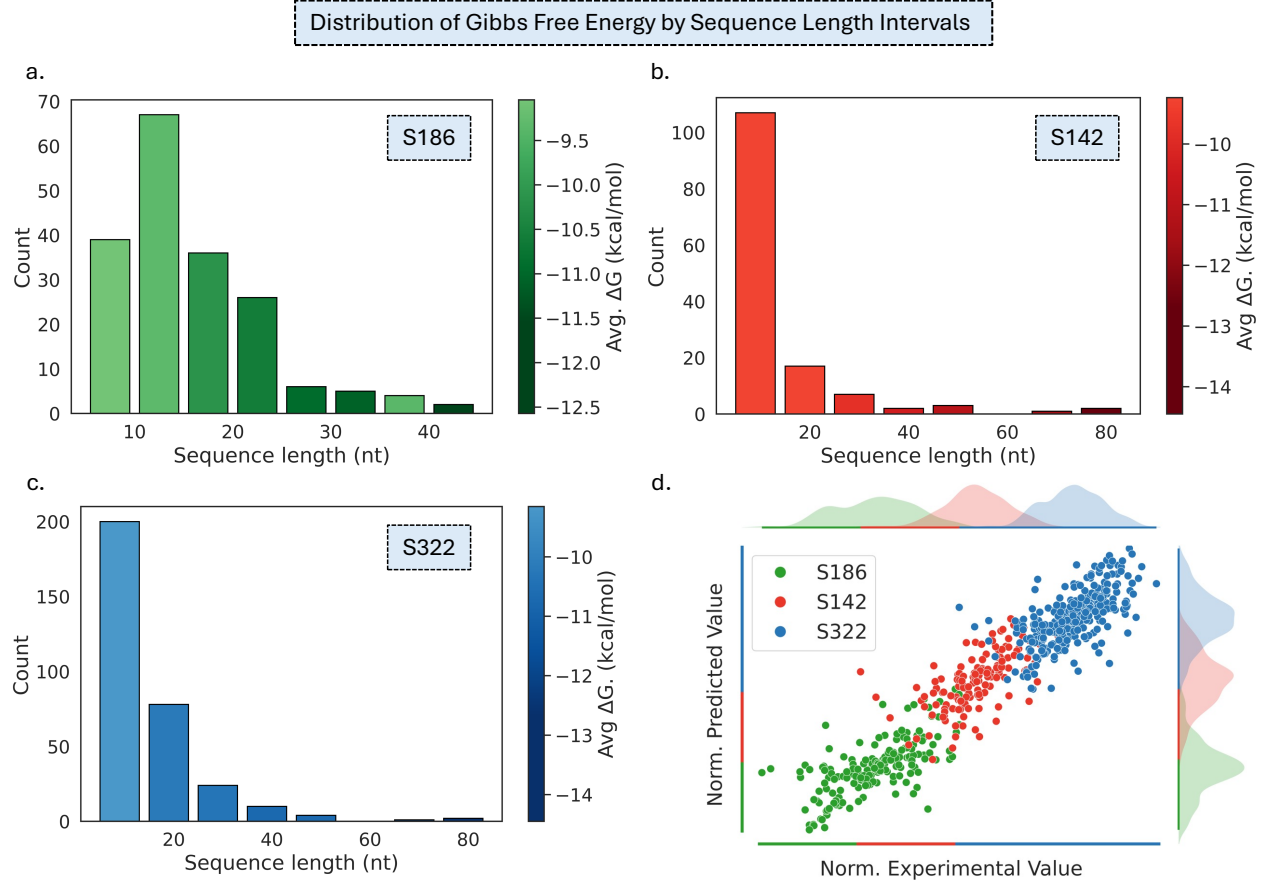


Figure 3: Distribution of experimental Gibbs free energy (ΔG) across sequence length intervals for the datasets (a) S186, (b) S142, and (c) S322. Color intensity encodes mean ΔG ; darker shades indicate stronger while lighter shades represents weaker binding. (d) A comparison of normalized experimental and predicted binding affinities of S186, S142, and S322 datasets. Each dataset is scaled to a specific region with an equal range for clear visual illustration.

It is evident that both datasets display a tendency toward more negative (stronger) experimental ΔG values as sequence length increases, despite sequence counts peaking at shorter lengths. An illustration of how binding free energy varies with sequence length in S142 is represented in Figure 3b. While the strand lengths range from 4~93~nt, we note that the mean affinity at the short end (4~nt), is -7.05 kcal/mol, whereas the longest RNAs (93~nt) bind much more strongly ($\Delta G = -12.27$ kcal/mol). Moreover, we also observe that most RNA complexes (107) fall in the 4-14~nt interval with a mean $\Delta G = -9.24$ kcal/mol. For the S322 dataset in Figure 3c, the shortest sequence in the dataset has experimental free-energy change spanning from -10.56 to -4.25 kcal/mol, with a mean of -7.05 kcal/mol. Conversely, the longest sequence in S322 is 93~nt and shows a single measured value of $\Delta G = -12.27$ kcal/mol. The mean ΔG for the length interval is -9.15 kcal/mol. Figure 3d juxtaposes the experimental and CAP-predicted binding affinities for the S186, S142, and S322 datasets. To aid visual comparison, the points from each dataset are rescaled to the same numerical range and plotted in separate, equally sized bands.

4 Methods

In this section, we provide an overview of persistent Stanley-Reisner theory (PSRT). Next, we describe the vectorization of persistent commutative algebra along with natural-language processing (NLP) method and model interpretability. Machine learning models and model evaluation metrics are also provided.

4.1 Persistent Stanley-Reisner Theory

Persistent Stanley-Reisner theory introduces a new framework for studying data geometry through combinatorial commutative algebra [39]. It maps input data to a simplicial complex made up of vertices, edges, triangles, and cells of higher dimension, thereby preserving both topological and combinatorial characteristics. A filtration records how these characteristics emerge and persist across different spatial scales, yielding algebraic invariants such as persistent facet ideals and adding an algebraic viewpoint to multiscale data analysis.

Let Δ be a simplicial complex on the vertex set $V = \{x_1, \dots, x_n\}$, and let $(\Delta^t)_{t \in \mathbb{R}}$ be a filtration such that $\Delta^s \subseteq \Delta^t$ whenever $s \leq t$. Fix a field k , and consider the polynomial ring $S := k[x_1, \dots, x_n]$. To each Δ^t , we associate the corresponding Stanley-Reisner ideal $I^t \subseteq S$, defined by

$$I^t := I(\Delta^t) := \langle x_{i_1} \cdots x_{i_r} \mid \{x_{i_1}, \dots, x_{i_r}\} \notin \Delta^t \rangle. \quad (1)$$

This construction yields a descending sequence of ideals as t increases.

Each ideal I^t admits a canonical primary decomposition into monomial prime ideals of the form

$$I^t = \bigcap_{\sigma \in \mathcal{F}(\Delta^t)} P_\sigma, \quad \text{where} \quad P_\sigma := (x_i \mid x_i \notin \sigma) \subseteq S,$$

and $\mathcal{F}(\Delta^t)$ denotes the set of facets of Δ^t . The ideals P_σ are referred to as the facet ideals at level t .

Let

$$\mathcal{P}^t := \{P_\sigma \mid \sigma \in \mathcal{F}(\Delta^t)\}$$

denote the set of facet ideals associated to Δ^t . To analyze the structure of \mathcal{P}^t by dimension, for each $i \geq 0$, define the graded stratification

$$\mathcal{P}_i^t := \{P_\sigma \in \mathcal{P}^t \mid \dim(\sigma) = i\},$$

so that

$$\mathcal{P}^t = \bigsqcup_{i=0}^{\dim(\Delta^t)} \mathcal{P}_i^t.$$

In analogy with persistent homology, we define the notion of persistent facet ideals and their associated facet persistent numbers. A facet ideal $P_\sigma \in \mathcal{P}_i^t$ is said to persist to level $t' > t$ if $P_\sigma \in \mathcal{P}_i^{t'}$. The set of such persistent i -dimensional facet ideals is denoted by

$$\mathcal{P}_i^{t,t'} := \mathcal{P}_i^t \cap \mathcal{P}_i^{t'}.$$

The corresponding facet persistent number is defined as

$$\mathcal{F}_i^{t,t'} := |\mathcal{P}_i^{t,t'}|,$$

which counts the number of i -dimensional facet ideals common to both levels t and t' .

The collection $\{\mathcal{F}_i^{t,t'}\}_{i,t,t'}$ defines a graded combinatorial invariant that captures the evolution of the minimal prime decompositions of the Stanley–Reisner ideals across the filtration. These invariants quantify the persistence of i -dimensional facet ideals and may be regarded as an algebraic counterpart to topological barcodes in persistent homology.

In the special case where $t = t'$, the function

$$t \mapsto \mathcal{F}_i^{t,t}$$

is referred to as the facet curve of degree i . It records the number of i -dimensional facet ideals appearing in the minimal prime decomposition of I^t at each level t .

Furthermore, the normalized quantity

$$\frac{\mathcal{F}_i^{t,t}}{t}$$

is called the persistence rate of the i th facet persistent number at time t , and serves as a measure of the density of i -dimensional prime components within the decomposition of I^t .

4.2 1-mer Algebra

In this section, we present the specialization of the k -mer algebra framework to the case $k = 1$. This method derives an algebraic structure through the Stanley–Reisner construction, based on the positional distribution of individual nucleotides. Let \mathcal{A} be $\{A, C, G, T/U\}$, and let

$$S = s_1 s_2 \cdots s_N \in \mathcal{A}^N$$

be a sequence of length N . For each letter $a \in \mathcal{A}$, define the indicator function

$$\delta_a: \mathcal{A} \rightarrow \{0, 1\}, \quad \delta_a(b) = \begin{cases} 1, & b = a, \\ 0, & b \neq a. \end{cases}$$

The set of positions at which a occurs in S is

$$S^a = \{i \in \{1, \dots, N\} \mid \delta_a(s_i) = 1\} \subset \mathbb{N}.$$

We view $S^a \subset \mathbb{R}$ as a one-dimensional input data. Define the corresponding pairwise distance matrix

$$D^a = (d_{ij}^a)_{i,j \in S^a} \in \mathbb{R}^{|S^a| \times |S^a|}, \quad d_{ij}^a = |i - j|.$$

Fix a filtration interval $[t_0, t_1] \subset \mathbb{R}_{\geq 0}$. For each $t \in [t_0, t_1]$, construct the Vietoris–Rips complex on S^a at scale t and compute its algebraic invariants. Denote by

$$v_a^t = (v_i^t(a))_{i \in \mathbb{N}}$$

the vector of algebraic invariants in each dimension $i \in \mathbb{N}$ (e.g. facet vectors \mathcal{F} , and facet rate vectors.). Restricting to a fixed scale t , we write

$$v_a := (v_i(a))_{i \in \mathbb{N}}.$$

Finally, the full 1-mer representation of S is obtained by concatenation over all $a \in \mathcal{A}$:

$$\mathbf{v}_S^1 := (v_a \mid a \in \mathcal{A}) = (\mathbf{v}_{S,i}^1)_{i \in \mathbb{N}},$$

where $\mathbf{v}_{S,i}^1 := (v_i(A), v_i(C), v_i(G), v_i(T/U))$ is the vector of dimension- i features computed over all 1-mers in S . We refer to \mathbf{v}_S^1 as the CAP-vector representation of S at $k = 1$, which encodes the spatial distribution of each symbol via persistent algebraic invariants.

4.3 Vectorization of persistent commutative algebra

To capture the intrinsic structure of nucleic acid sequence, we encode every sequence as a one-dimensional input data, where each point indicates the position of a mononucleotide (i.e., k -mers of length 1). To ensure consistency, we applied a uniform grid of fifty equally spaced filtration thresholds, $r = 0, 1, 2, \dots, 49$, to every k -mer input. A Vietoris-Rips filtration is then applied using these fixed radii across all samples. This setup generates uniformly aligned facet-count curves and their corresponding rate profiles, each sampled at fifty evenly spaced filtration values. As a result, we derive two parallel families of features with a filtration design that captures structural regularities while suppressing noise and guarding against outliers.

For each sequence, we identify the positions of all four mononucleotides (A, C, G, T/U), forming four separate inputs. To each input, we apply persistent commutative algebra modeling, using persistent facet ideals to measure the algebraic complexity of interaction structures across scales. For every mononucleotide-specific cloud, we compute 50-dimensional facet curves in dimensions 0, 1, and 2, along with 50-dimensional rate curves capturing the change in facet growth across the filtration. This yields 150 features from the facet counts and 150 from the facet rates, resulting in 300 features per nucleotide. Concatenating the features across all four nucleotide types produces a 1200-dimensional feature vector that summarizes sequence-derived structural patterns. This coherent representation of simplicial structure and connectivity evolution across an identical filtration range yields a rich input for our binding-affinity model.

4.4 Transformer-based protein language model

Recent advances in natural-language processing (NLP) provide powerful sequence-based insights for molecular biosciences. We harness these techniques to augment our PSRT framework for predicting protein-nucleic acid binding affinities. While PSRT analyzes nucleic acid sequences, NLP captures patterns directly from amino acid sequences.

To complement the commutative-algebraic descriptors of DNA/RNA, we incorporate protein sequence information using a state-of-the-art transformer-based language model, ESM2 [15]. This model processes the raw amino acid sequence and outputs 2560-dimensional high-level embeddings by aggregating across 36 transformer layers. The final feature matrix for each protein-nucleic acid complex is constructed by concatenating the 1200-dimensional PCA-derived nucleotide features with the 2560-dimensional ESM2-based protein features, resulting in a unified 3760-dimensional

representation. These composite features are used to train and evaluate CAP on our dataset. An illustration of the workflow in CAP is demonstrated in Figure 1.

4.5 Machine learning modeling

We train our regression models with Gradient Boosting Decision Trees (GBDT), implemented in Python via the `scikit-learn` library (v1.3.2). GBDT is valued for its resistance to overfitting, limited sensitivity to hyperparameter tuning, and straightforward deployment. It assembles many shallow decision trees generated from bootstrap samples of the training data and aggregates their outputs, so the ensemble corrects errors that any single tree might make. We supply the algorithm separately with PSRT-derived molecular descriptors and transformer-based descriptors; the hyperparameter settings are listed in Table 3.

Table 3: Hyperparameters used in the gradient boosting regression model within a scikit-learn pipeline. StandardScaler is applied prior to model training.

No. of estimators	Max depth	Min. samples split	Learning rate
10,000	7	3	0.01
Max features	Subsample size	Random state	Standardization
Square root	0.7	Fixed (seeded)	Yes (StandardScaler)

4.6 Evaluation metrics

To quantitatively evaluate the performance of our binding affinity prediction models, we employ the Pearson correlation coefficient (*PCC*), defined as:

$$\text{PCC}(\mathbf{x}, \mathbf{y}) = \frac{\sum_{m=1}^M (y_m^e - \bar{y}^e)(y_m^p - \bar{y}^p)}{\sqrt{\sum_{m=1}^M (y_m^e - \bar{y}^e)^2 \sum_{m=1}^M (y_m^p - \bar{y}^p)^2}},$$

where y_m^e and y_m^p denote the experimental and predicted binding affinity values for the m -th sample, respectively, and \bar{y}^e and \bar{y}^p are their corresponding mean values.

We also report the root mean squared error (RMSE), which is computed as:

$$\text{RMSE} = \sqrt{\frac{1}{n} \sum_{m=1}^M (y_m^e - y_m^p)^2},$$

where y_m^e and y_m^p represent the experimental and predicted binding affinity values for the m -th sample, respectively.

The above two metrics are employed to assess the performance of our machine learning models on all datasets. The original labels for these datasets are given as pK_d values, which are converted to binding free energies (in kcal/mol) by multiplying by a constant factor of 1.3633. Our models achieve reasonable RMSE values across all three datasets.

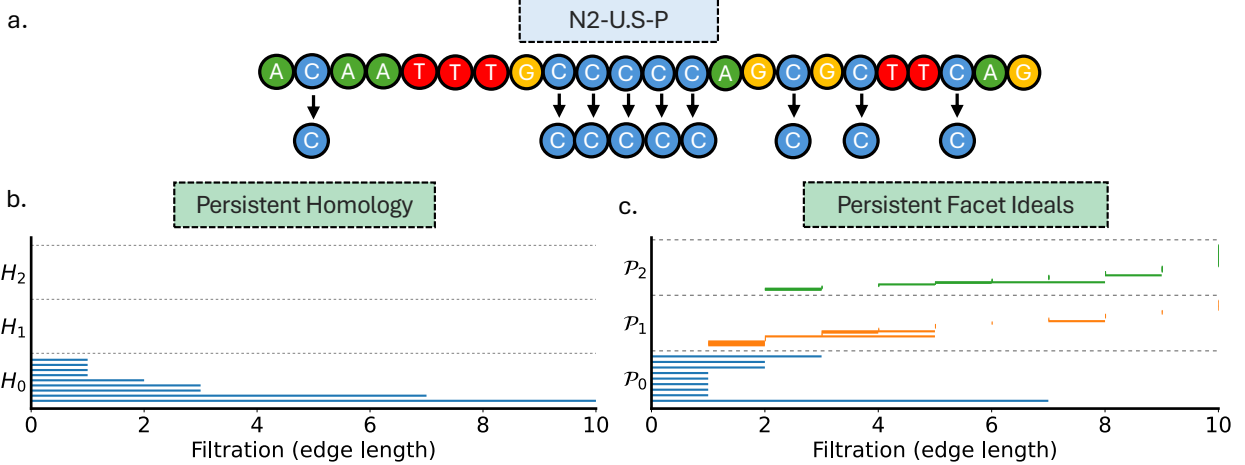


Figure 4: Comparison between Persistent Homology and Persistent Stanley-Reisner Invariants. (a) The N2-U-S-P primer sequence, with the positions of the nucleotide C marked. (b) The persistent homology barcodes computed from the input set formed by the positions of C, representing topological features in the spatial distribution. (c) The persistent facet barcodes derived of the same input set, encoding combinatorial face-level patterns rather than topological invariants and reflecting the algebraic invariants of maximal simplices under the same induced filtration.

5 Model interpretability

Topological techniques like persistent homology (PH) [45] and persistent Laplacian theory [46] have emerged as powerful tools in machine learning frameworks. Although our persistent commutative algebra technique is built on the same simplicial-complex scaffold of PH however, it unravels the combinatorial activity by shifting the focus from a global view to a fine-grained, local view across the same filtration. Moreover, in comparison with persistent Laplacian theory [46], which can be computationally intensive in terms of analyzing eigenvalues of large Laplacian matrices, our algebraic construction sidesteps matrix diagonalization and scales more efficiently. Each of these varying paradigms offers its own unique advantages, making them suitable for different data regimes and analytical goals.

In this section, we demonstrate how a simplicial complex evolves distinctively under a growing filtration parameter for PH and persistent Stanley-Reisner (SR) approach. For this purpose, we analyze the N2-U-S-P primer sequence as shown in Figure 4a. The 23-nucleotide primer contains several cytosines that we have highlighted; only these C residues are used to build the one-dimensional input set in this example, placing each point at its sequence index (positions 2, 9, 10, 11, 12, 13, 16, 18, and 21). This resulting input set is analyzed using both persistent homology and persistent facet ideals.

Figure 4b shows the barcodes from the persistent homology analysis, which records the appearance and disappearance of global features - connected components, loops, and voids - as the Vietoris–Rips filtration radius r increases. For this cytosine-based one-dimensional input, the H_0 barcode comprises blue bars, each initially representing an isolated cytosine at $r = 0$. As the filtration expands, these points progressively merge, reducing the number of separate clusters. Notably, no bars appear in the H_1 or H_2 lanes, indicating that higher-dimensional features such as loops and cavities are

not formed in this case. On the contrary, Figure 4c shows barcodes derived from the persistent facet ideals applied to the same filtration data. The zeroth-dimensional panel P_0 barcodes (blue bars) shows the appearance of isolated components. The edges appear around $r = 1$ in the first-dimensional panel P_1 (orange bars) which was entirely missed by persistent homology. Similarly, the second-dimensional panel P_2 (green bars) captures the birth and death of 2-simplices around $r = 2$, indicating the formation of triangular faces in the structure as the filtration progresses.

Persistent homology and persistent facet ideals both analyze how a simplicial complex evolves under a growing filtration parameter, but they focus on different features. Unlike persistent homology which is summarized by the Betti-number barcodes, persistent facet ideals directly capture local simplex activities (vertices, edges, triangles, and higher-order structures) throughout the filtration process. The filtration process involves gradually increasing a radius parameter r to monitor the formation and dissolution of topological features encoded via facet ideals. For example, the H_0 barcode records the number of connected components: it begins at the total number of vertices and decreases by one each time an edge appears, reaching a single component when the complex becomes fully connected. In contrast, the facet-ideal count P_0 measures the number of isolated vertices (0-simplices not yet incident to any edge) and thus falls to zero as soon as every vertex participates in at least one edge. This facet-based barcode framework captures both geometric and combinatorial properties of molecules. Thus, persistent homology emphasizes the emergence of homology classes that change the global topology, while persistent facet ideals specialize in capturing precise local combinatorial events across the same filtration. This enhances interpretability and relevance for biomolecular sequence analyses, thereby improving subsequent performance in machine learning applications.

6 Conclusion

Commutative algebra, traditionally central to fields like algebraic geometry and number theory, has remained largely untapped in data-driven and biological research. Recent work by Suwayyid and Wei [39] changes this by integrating Stanley-Reisner theory with multiscale analysis, opening a new avenue for nonlinear algebraic techniques in data science. Initial studies, such as those on protein-ligand binding affinity [40], attest to the power of the persistent Stanley-Reisner theory (PSRT) framework for enhancing machine learning models.

In this work, we present commutative algebra prediction (CAP), a framework for protein-nucleic acid binding affinity prediction that integrates PSRT-based k -mer algebra descriptors of DNA sequences and transformer-derived ESM2 embeddings of protein sequences. We evaluate the performance of our model on the S186 dataset with an additional test on newly curated datasets S142 and S322. CAP is trained with a single gradient-boosting regression tree model to provide variance across splits without the need for iterative feature pruning or subclass-specific retraining. Our findings deliver strong and generalizable predictions with Pearson correlation coefficient of 0.705 with RMSE of 1.79 kcal/mol outperforming SVSBI [11] (0.669/1.98 kcal/mol). Furthermore, CAP attains a PCC of 0.653 and an RMSE of 2.18 kcal/mol on S142, while its performance improves on S322, reaching a PCC of 0.669 with an RMSE of 2.0 kcal/mol. These results demonstrate the robustness of CAP in jointly capturing informative DNA k -mer algebra signatures and protein ESM2 embeddings, thereby enabling reliable prediction of protein-nucleic acid binding affinities. Finally, because CAP’s inputs are limited to primary sequences, the framework is inherently scalable: it can be applied to any protein-DNA/RNA pair with minimal preprocessing and is readily extensible

to genome-scale studies. In addition to this, the proposed commutative algebraic methodology can not only be applied to the study of other biological sequences, such as phylogenetic analysis and protein sequence representation but it can also be generalized to the analysis of other sequential data in science and engineering.

Data and Code availability

All codes and datasets needed to evaluate the conclusions in this study are available at <https://github.com/mzias/CAP>. The SVSBI dataset can also be accessed at <https://github.com/WeilabMSU/SVS>.

Supporting Information

Supplementary Information is available for supplementary tables.

Conflict of Interest

The authors declare no competing financial interests.

Acknowledgments

This work was supported in part by NIH grant R35GM148196, NSF grant DMS-2052983, and MSU Research Foundation. F.S. thanks King Fahd University of Petroleum and Minerals for their support.

References

- [1] Jean B Bertoldo, Simon Müller, and Stefan Hüttelmaier. Rna-binding proteins in cancer drug discovery. *Drug discovery today*, 28(6):103580, 2023.
- [2] Glen E Kisby, David M Wilson III, and Peter S Spencer. Introducing the role of genotoxicity in neurodegenerative diseases and neuropsychiatric disorders. *International journal of molecular sciences*, 25(13):7221, 2024.
- [3] Peter G Stockley. Filter-binding assays. *DNA-Protein Interactions: Principles and Protocols, Third Edition*, pages 1–14, 2009.
- [4] Chi Zhang, Song Liu, Qianqian Zhu, and Yaoqi Zhou. A knowledge-based energy function for protein- ligand, protein- protein, and protein- dna complexes. *Journal of medicinal chemistry*, 48(7):2325–2335, 2005.
- [5] Chandran Nithin, Sunandan Mukherjee, and Ranjit Prasad Bahadur. A structure-based model for the prediction of protein–rna binding affinity. *RNA*, 25(12):1628–1645, 2019.
- [6] Shuangye Yin, Lada Biedermannova, Jiri Vondrasek, and Nikolay V Dokholyan. Medusascore: an accurate force field-based scoring function for virtual drug screening. *Journal of chemical information and modeling*, 48(8):1656–1662, 2008.
- [7] Gabriela Bitencourt-Ferreira and Walter Filgueira de Azevedo Jr. Machine learning to predict binding affinity. In *Docking Screens for Drug Discovery*, pages 251–273. Springer, 2019.
- [8] Markus Hafner, Markus Landthaler, Lukas Burger, Mohsen Khorshid, Jean Hausser, Philipp Berninger, Andrea Rothballer, Manuel Ascano, Anna-Carina Jungkamp, Mathias Munschauer, et al. Transcriptome-wide identification of rna-binding protein and microrna target sites by par-clip. *Cell*, 141(1):129–141, 2010.
- [9] Huiying Zhao, Yuedong Yang, and Yaoqi Zhou. Structure-based prediction of rna-binding domains and rna-binding sites and application to structural genomics targets. *Nucleic acids research*, 39(8):3017–3025, 2011.
- [10] Zhi-Ping Liu and Hongyu Miao. Prediction of protein-rna interactions using sequence and structure descriptors. *Neurocomputing*, 206:28–34, 2016.
- [11] Li Shen, Hongsong Feng, Yuchi Qiu, and Guo-Wei Wei. Svsbi: sequence-based virtual screening of biomolecular interactions. *Communications biology*, 6(1):536, 2023.
- [12] Irina Tuszynska and Janusz M Bujnicki. Dars-rnp and quasi-rnp: new statistical potentials for protein-rna docking. *BMC bioinformatics*, 12:1–16, 2011.
- [13] Piotr Setny and Martin Zacharias. A coarse-grained force field for protein–rna docking. *Nucleic acids research*, 39(21):9118–9129, 2011.
- [14] Junichi Iwakiri, Michiaki Hamada, Kiyoshi Asai, and Tomoshi Kameda. Improved accuracy in rna–protein rigid body docking by incorporating force field for molecular dynamics simulation into the scoring function. *Journal of chemical theory and computation*, 12(9):4688–4697, 2016.

- [15] Zeming Lin, Halil Akin, Roshan Rao, Brian Hie, Zhongkai Zhu, Wenting Lu, Nikita Smetanin, Robert Verkuil, Ori Kabeli, Yaniv Shmueli, et al. Evolutionary-scale prediction of atomic-level protein structure with a language model. *Science*, 379(6637):1123–1130, 2023.
- [16] Yao Song and Lu Wang. Multiobjective tree-based reinforcement learning for estimating tolerant dynamic treatment regimes. *Biometrics*, 80(1):ujad017, 2024.
- [17] Yu-Chen Lo, Stefano E Rensi, Wen Torng, and Russ B Altman. Machine learning in chemoinformatics and drug discovery. *Drug discovery today*, 23(8):1538–1546, 2018.
- [18] Zixuan Cang and Guo-Wei Wei. Topologynet: Topology based deep convolutional and multi-task neural networks for biomolecular property predictions. *PLoS computational biology*, 13(7):e1005690, 2017.
- [19] Theodore Papamarkou, Tolga Birdal, Michael Bronstein, Gunnar Carlsson, Justin Curry, Yue Gao, Mustafa Hajij, Roland Kwitt, Pietro Lio, Paolo Di Lorenzo, et al. Position: Topological deep learning is the new frontier for relational learning. *Proceedings of machine learning research*, 235:39529, 2024.
- [20] Duc Duy Nguyen, Zixuan Cang, and Guo-Wei Wei. A review of mathematical representations of biomolecular data. *Physical Chemistry Chemical Physics*, 22(8):4343–4367, 2020.
- [21] Kamal Rana. *The Geometry and Topology of Landslides*. Rochester Institute of Technology, 2023.
- [22] Yaxing Wang, Xiang Liu, Yipeng Zhang, Xiangjun Wang, and Kelin Xia. Join persistent homology (jph)-based machine learning for metalloprotein–ligand binding affinity prediction. *Journal of Chemical Information and Modeling*, 65(6):2785–2793, 2025.
- [23] Duc Duy Nguyen, Zixuan Cang, Kedi Wu, Menglun Wang, Yin Cao, and Guo-Wei Wei. Mathematical deep learning for pose and binding affinity prediction and ranking in d3r grand challenges. *Journal of computer-aided molecular design*, 33:71–82, 2019.
- [24] Duc Duy Nguyen, Kaifu Gao, Menglun Wang, and Guo-Wei Wei. Mathdl: mathematical deep learning for d3r grand challenge 4. *Journal of computer-aided molecular design*, 34(2):131–147, 2020.
- [25] Yuta Hozumi and Guo-Wei Wei. Revealing the shape of genome space via k-mer topology. *arXiv preprint arXiv:2412.20202*, 2024.
- [26] Jian Liu, Li Shen, Dong Chen, and Guo-Wei Wei. Topological sequence analysis of genomes: Delta complex approaches. *arXiv preprint arXiv:2507.05452*, 2025.
- [27] Jian Liu, Li Shen, Mushal Zia, and Guo-Wei Wei. Topological sequence analysis of genomes: Category approaches. *arXiv preprint arXiv:2507.08043*, 2025.
- [28] Huiying Zhao, Yuedong Yang, and Yaoqi Zhou. Structure-based prediction of dna-binding proteins by structural alignment and a volume-fraction corrected dfire-based energy function. *Bioinformatics*, 26(15):1857–1863, 2010.
- [29] Chaitanya Rastogi, H Tomas Rube, Judith F Kribelbauer, Justin Crocker, Ryan E Loker, Gabriella D Martini, Oleg Laptenko, William A Freed-Pastor, Carol Prives, David L Stern, et al. Accurate and sensitive quantification of protein-dna binding affinity. *Proceedings of the National Academy of Sciences*, 115(16):E3692–E3701, 2018.

[30] Sandro Barissi, Alba Sala, Miłosz Wieczór, Federica Battistini, and Modesto Orozco. Dnaffinity: a machine-learning approach to predict dna binding affinities of transcription factors. *Nucleic Acids Research*, 50(16):9105–9114, 2022.

[31] Wenyi Yang and Lei Deng. Predba: a heterogeneous ensemble approach for predicting protein-dna binding affinity. *Scientific reports*, 10(1):1278, 2020.

[32] K Harini, Daisuke Kihara, and M Michael Gromiha. Pda-pred: Predicting the binding affinity of protein-dna complexes using machine learning techniques and structural features. *Methods*, 213:10–17, 2023.

[33] Shuang Yang, Weikang Gong, Tong Zhou, Xiaohan Sun, Lei Chen, Wenxue Zhou, and Chunhua Li. empdba: protein-dna binding affinity prediction by combining features from binding partners and interface learned with ensemble regression model. *Briefings in Bioinformatics*, 24(4):bbad192, 2023.

[34] Xiufeng Yang, Haotian Li, Yangyu Huang, and Shiyong Liu. The dataset for protein–rna binding affinity. *Protein Science*, 22(12):1808–1811, 2013.

[35] Lei Deng, Wenyi Yang, and Hui Liu. Predprba: prediction of protein-rna binding affinity using gradient boosted regression trees. *Frontiers in genetics*, 10:637, 2019.

[36] Xu Hong, Xiaoxue Tong, Juan Xie, Pinyu Liu, Xudong Liu, Qi Song, Sen Liu, and Shiyong Liu. An updated dataset and a structure-based prediction model for protein–rna binding affinity. *Proteins: Structure, Function, and Bioinformatics*, 91(9):1245–1253, 2023.

[37] K Harini, M Sekijima, and M Michael Gromiha. Pra-pred: Structure-based prediction of protein-rna binding affinity. *International Journal of Biological Macromolecules*, 259:129490, 2024.

[38] David Eisenbud. *Commutative algebra: with a view toward algebraic geometry*, volume 150. Springer Science & Business Media, 2013.

[39] Faisal Suwayyid and Guo-Wei Wei. Persistent stanley–reisner theory. *arXiv preprint arXiv:2503.23482*, 2025.

[40] Hongsong Feng, Faisal Suwayyid, Mushal Zia, JunJie Wee, Yuta Hozumi, Chun-Long Chen, and Guo-Wei Wei. Caml: Commutative algebra machine learning—a case study on protein–ligand binding affinity prediction. *Journal of Chemical Information and Modeling*, 2025.

[41] Richard P Stanley. *Combinatorics and commutative algebra*, volume 41. Springer Science & Business Media, 2007.

[42] Christopher A Francisco, Jeffrey Mermin, and Jay Schweig. A survey of stanley–reisner theory. In *Connections between algebra, combinatorics, and geometry*, pages 209–234. Springer, 2014.

[43] Meredith Corley, Margaret C Burns, and Gene W Yeo. How rna-binding proteins interact with rna: molecules and mechanisms. *Molecular cell*, 78(1):9–29, 2020.

[44] Dhanusha Yesudhas, Maria Batool, Muhammad Ayaz Anwar, Suresh Panneerselvam, and Sangdun Choi. Proteins recognizing dna: Structural uniqueness and versatility of dna-binding domains in stem cell transcription factors. *Genes*, 8(8):192, 2017.

- [45] Afra Zomorodian and Gunnar Carlsson. Computing persistent homology. In *Proceedings of the twentieth annual symposium on Computational geometry*, pages 347–356, 2004.
- [46] Rui Wang, Duc Duy Nguyen, and Guo-Wei Wei. Persistent spectral graph. *International journal for numerical methods in biomedical engineering*, 36(9):e3376, 2020.

Supporting Information

CAP: Commutative Algebra Prediction of Protein-Nucleic Acid Binding Affinities

Mushal Zia¹, Faisal Suwayyid ^{1,2}, Yuta Hozumi* ¹
JunJie Wee¹, Hongsong Feng³, and Guo-Wei Wei^{†1,4,5}

¹Department of Mathematics,
Michigan State University, MI 48824, USA.

King Fahd University of Petroleum and Minerals, Dhahran 31261, KSA.

³Department of Mathematics and Statistics,
University of North Carolina at Charlotte, Charlotte, NC 28223, USA

⁴Department of Electrical and Computer Engineering,
Michigan State University, MI 48824, USA.

⁵Department of Biochemistry and Molecular Biology,
Michigan State University, MI 48824, USA.

*Current address: School of Mathematics, Georgia Institute of Technology, Atlanta, GA, USA.

†Corresponding author: Guo-Wei Wei (weig@msu.edu).

Contents

1 Results: Experimental vs. Predicted Binding Affinities	2
1.1 The S186 Dataset	2
1.2 The S142 Dataset	4
1.3 The S322 Dataset	6

1 Results: Experimental vs. Predicted Binding Affinities

1.1 The S186 Dataset

Table S1: Experimental and predicted binding free energies (ΔG) for the S186 dataset [?].

PDBID	Exp BA	Pred BA	PDBID	Exp BA	Pred BA	PDBID	Exp BA	Pred BA
1HVO	-6.760	-7.227	1WET	-7.940	-11.516	2PUF	-7.769	-11.158
1QPZ	-11.704	-10.246	1QP0	-10.165	-10.955	1QP7	-8.327	-8.392
1FJX	-12.070	-12.671	1J75	-10.165	-9.392	1JFS	-11.803	-10.957
1J5K	-7.529	-9.805	1PO6	-9.276	-9.696	1P51	-11.528	-11.390
1QZG	-8.614	-9.464	1OSB	-9.754	-9.754	1HVN	-7.227	-6.758
1BDH	-8.242	-8.118	1QP4	-10.906	-11.221	1QQB	-7.769	-8.664
1TW8	-12.192	-12.234	1QQA	-8.722	-8.250	1DH3	-12.070	-10.448
1JJ4	-11.991	-10.913	1FYM	-10.086	-9.559	1JH9	-11.859	-7.913
1JT0	-9.965	-10.387	1P78	-11.528	-11.555	1P71	-11.528	-11.296
1OMH	-9.754	-9.754	1S40	-12.983	-10.193	1U1L	-9.503	-8.938
1U1R	-9.053	-9.165	1U1N	-8.862	-9.677	1U1O	-9.855	-9.646
2BJC	-14.996	-10.129	1ZZI	-7.713	-9.770	2B0D	-8.242	-9.134
2GII	-12.783	-12.781	2GIE	-12.592	-12.582	2GIH	-12.252	-12.254
2ADY	-10.707	-10.494	2AC0	-10.364	-10.013	2AYB	-11.859	-11.797
2ERE	-10.256	-10.295	2GE5	-8.751	-9.147	2O6M	-10.751	-10.058
3D6Z	-8.204	-6.798	2VYE	-9.991	-9.671	3IGM	-8.590	-9.391
3HXQ	-12.572	-12.566	3EQT	-9.514	-9.864	3H15	-7.455	-8.684
2KAE	-11.039	-9.858	3MQ6	-12.572	-10.865	3JSP	-11.995	-12.031
3AAF	-8.994	-9.236	3N1L	-11.407	-11.239	3N1K	-11.236	-11.406
3R8F	-9.487	-9.775	2RRA	-7.940	-9.453	3QMI	-6.709	-6.639
2KXN	-7.700	-9.556	1U1P	-9.107	-9.274	1U1M	-8.901	-9.165
1U1K	-8.856	-9.141	1U1Q	-9.706	-9.586	2AOR	-8.242	-8.299
2AOQ	-7.438	-8.094	2I9K	-12.983	-11.832	2GIJ	-12.783	-12.781
2GIG	-12.252	-12.254	2CCZ	-9.543	-10.346	2AHI	-10.496	-10.705
2ERG	-10.364	-10.034	2AYG	-11.859	-11.765	2ES2	-8.843	-9.358
2ATA	-9.646	-10.400	2NP2	-9.897	-10.567	3D6Y	-6.799	-8.206
2VY1	-9.573	-9.888	3HXO	-12.572	-12.572	3GIB	-12.070	-9.482
3D2W	-9.355	-9.032	2KKF	-5.939	-7.859	3M9E	-9.388	-9.799
3JSO	-12.402	-11.641	3K3R	-11.966	-12.244	3N1I	-11.554	-10.859
3N1J	-11.386	-10.859	3KJP	-11.180	-9.631	3Q0B	-8.134	-9.231
3PIH	-11.890	-10.408	3QMH	-6.502	-6.823	3QMB	-7.438	-6.574

PDBID	Exp BA	Pred BA	PDBID	Exp BA	Pred BA	PDBID	Exp BA	Pred BA
3U7F	-8.482	-9.231	3RN2	-9.476	-9.011	4ATK	-11.956	-11.850
2LTT	-10.628	-10.156	4HIO	-10.467	-10.106	4HIK	-10.388	-10.374
4A76	-9.855	-9.274	4HJ7	-11.209	-10.445	4HID	-8.273	-10.424
4LJ0	-8.590	-9.187	4HT8	-9.471	-11.451	4GCK	-9.256	-9.742
4F2J	-10.364	-10.110	4GCT	-9.915	-9.872	4NI7	-13.223	-9.962
4CH1	-9.003	-9.149	4QJU	-8.768	-10.589	4ZBN	-13.194	-10.142
4R55	-7.876	-9.658	4S0N	-10.751	-9.311	4ZSF	-11.639	-10.816
4RKG	-6.258	-9.099	5A72	-9.916	-10.327	5DWA	-12.332	-10.915
5K83	-7.913	-6.797	5ITH	-10.256	-9.518	5W9S	-9.543	-8.161
5YI3	-8.534	-9.730	5XFP	-8.072	-9.584	5MEY	-9.265	-9.084
5MEZ	-9.001	-9.356	5W2M	-7.084	-7.453	5K17	-6.891	-9.412
6MG1	-10.276	-11.106	5VMV	-12.769	-10.045	6CNQ	-8.242	-9.063
6FQP	-9.229	-9.342	5WWF	-9.029	-9.040	6FQQ	-8.739	-9.349
5ZVB	-5.990	-5.940	5ZVA	-5.809	-6.266	5MPF	-9.605	-9.887
6G1L	-12.332	-11.459	6IIQ	-8.024	-9.616	6IIR	-7.570	-9.127
3ON0	-11.341	-10.466	4HQU	-14.586	-11.900	4HQX	-12.162	-13.442
4A75	-9.232	-9.818	3QSU	-10.511	-10.019	4HJ8	-10.440	-8.511
4HIM	-10.132	-10.470	4HJ5	-9.817	-10.383	4HP1	-7.028	-8.751
4J1J	-8.584	-10.111	4NM6	-8.140	-9.119	4GCL	-9.278	-9.826
3ZPL	-11.751	-10.355	3ZH2	-10.057	-10.866	4HT4	-11.039	-9.790
4LNQ	-8.011	-9.152	4LJR	-10.244	-10.216	4R56	-9.370	-6.700
4TMU	-12.030	-7.978	4R22	-10.819	-10.223	4Z3C	-7.661	-8.187
3WPC	-10.496	-11.437	3WPD	-11.619	-10.389	2N8A	-9.573	-9.650
5HRT	-12.114	-10.186	5T1J	-10.526	-9.908	5VC9	-9.265	-7.710
5HLG	-8.873	-10.191	5W9Q	-8.482	-7.733	6ASB	-7.940	-9.008
6ASD	-7.661	-8.559	5K07	-6.122	-9.359	5YI2	-9.738	-8.594
6MG3	-11.449	-10.330	6FWR	-8.873	-10.244	6CNP	-8.391	-8.553
5ZD4	-10.798	-9.562	5ZMO	-9.163	-9.907	6BWY	-6.251	-9.430
6CRM	-7.264	-11.533	6CC8	-7.181	-9.183	6BUX	-5.807	-8.405
6A2I	-8.701	-7.031	5ZKI	-8.015	-10.158	6KBS	-7.713	-9.911
5ZKL	-10.479	-10.177	5ZMD	-7.407	-9.448	6ON0	-9.605	-9.688

1.2 The S142 Dataset

Table S2: Experimental and predicted binding free energies (ΔG) for the S142 dataset.

PDBID	Exp BA	Pred BA	PDBID	Exp BA	Pred BA	PDBID	Exp BA	Pred BA
2A9X	-9.303	-10.928	3BX3	-9.874	-10.332	3IRW	-14.996	-11.417
3IWN	-12.270	-13.614	3K0J	-10.992	-13.009	3QGB	-11.528	-11.324
2XS2	-10.113	-7.450	3QGC	-10.982	-10.932	4GHA	-8.590	-9.752
3V6Y	-11.464	-11.571	2LUP	-6.090	-10.548	4M59	-9.531	-12.045
2MTV	-9.526	-7.434	4RCM	-6.350	-8.934	5EIM	-8.123	-8.661
5GXH	-7.661	-9.294	5KLA	-10.334	-11.841	5EN1	-8.942	-8.889
5F5H	-9.668	-9.571	5WZK	-9.265	-10.337	5HO4	-9.462	-9.306
5U9B	-9.388	-8.770	5WZJ	-10.751	-10.317	5TF6	-11.639	-10.081
5SZE	-10.459	-8.724	5WZG	-10.218	-10.508	5M8I	-5.736	-8.548
5UDZ	-9.592	-9.059	5YTV	-8.043	-7.852	6FQ3	-8.015	-9.048
5YTX	-8.007	-8.022	5YKI	-12.030	-9.858	6DCL	-10.647	-9.134
6GD3	-5.191	-6.956	6G2K	-6.427	-6.652	6CMN	-11.727	-9.367
5YTS	-7.577	-7.648	5WWG	-9.077	-8.823	5WWF	-9.029	-8.892
5YTT	-7.394	-7.691	6FQR	-6.073	-7.340	6GX6	-7.264	-6.194
5WWE	-8.550	-9.024	6GC5	-8.435	-6.979	6RT6	-6.755	-7.770
6NOF	-10.617	-10.477	6R7B	-10.558	-9.084	6NOC	-10.490	-10.527
6NOH	-10.421	-10.602	6A6J	-9.068	-8.372	6NOD	-10.280	-11.359
6G99	-6.176	-9.008	6RT7	-7.405	-7.234	6U9X	-10.086	-9.895
6NY5	-9.952	-10.127	6GBM	-5.556	-9.515	1EC6	-7.990	-8.866
1M8Y	-9.270	-12.410	1RPU	-13.300	-9.820	1UTD	-16.890	-8.985
2B6G	-10.600	-9.754	2ERR	-12.200	-8.668	2F8K	-10.300	-9.725
2G4B	-7.830	-7.809	2KFY	-8.840	-8.056	2KG0	-7.400	-8.786
2KG1	-7.450	-8.247	2KX5	-11.400	-10.733	2KXN	-8.170	-8.775
2L41	-4.250	-7.057	2LA5	-11.500	-10.957	2LEB	-9.320	-9.455
2LEC	-9.440	-9.339	2M8D	-8.730	-8.857	2MJH	-9.670	-9.264
2MXY	-7.900	-6.836	2MZ1	-6.870	-7.886	2N82	-10.300	-9.827
2RRA	-7.940	-8.220	2RU3	-8.520	-9.256	2XC7	-7.040	-8.121
2XFM	-8.240	-7.664	2XNR	-5.400	-7.537	2ZKO	-8.050	-10.836
3BSB	-10.200	-10.686	3BSX	-11.500	-11.098	3BX2	-9.970	-9.783
3EQT	-9.520	-9.285	3GIB	-10.690	-9.402	3K49	-12.050	-10.730
3K4E	-10.800	-11.844	3K5Q	-9.300	-9.172	3K5Y	-10.540	-9.425
3K5Z	-9.380	-9.951	3K61	-8.890	-9.677	3K62	-8.740	-9.250
3K64	-9.220	-8.941	3L25	-8.175	-9.291	3LQX	-12.220	-10.107
3MDG	-7.850	-8.737	3MOJ	-13.000	-10.506	3NCU	-10.300	-9.229

PDBID	Exp BA	Pred BA	PDBID	Exp BA	Pred BA	PDBID	Exp BA	Pred BA
3NMR	-8.440	-7.356	3NNH	-6.190	-8.264	3O3I	-6.520	-7.069
3O6E	-7.070	-6.522	3Q0L	-12.300	-11.270	3Q0M	-12.500	-12.366
3Q0N	-10.500	-10.977	3Q0P	-12.800	-10.299	3Q0Q	-13.300	-12.526
3Q0R	-13.800	-12.844	3Q0S	-10.800	-12.416	3QG9	-10.600	-10.987
3U4M	-15.900	-10.326	3V71	-11.100	-10.255	3V74	-11.600	-11.382
3WBM	-9.980	-10.926	4CIO	-9.760	-8.359	4ED5	-9.080	-8.344
4ERD	-9.540	-9.409	4HT8	-9.380	-10.205	4Jvh	-9.590	-9.179
4KJI	-8.940	-10.087	4LG2	-9.540	-9.117	4NL3	-7.380	-10.254
4O26	-8.200	-11.597	4OE1	-12.110	-9.503	4QI2	-9.440	-9.509
4QVC	-11.560	-10.060	4QVD	-10.120	-10.314	4R3I	-7.770	-6.755
4RCJ	-8.180	-8.213	4TUX	-10.400	-9.475	4U8T	-9.130	-7.535
4Z31	-8.790	-9.061	5DNO	-7.830	-8.431	5ELR	-6.250	-8.894
5V7C	-6.990	-8.994	5W1I	-12.790	-10.833	5WZH	-10.460	-10.535
6D12	-9.300	-10.184						

1.3 The S322 Dataset

Table S3: Experimental and predicted binding free energies (ΔG) for the S322 dataset.

PDBID	Exp BA	Pred BA	PDBID	Exp BA	Pred BA	PDBID	Exp BA	Pred BA
1HVO	-6.760	-7.223	1WET	-7.940	-11.499	2PUF	-7.769	-10.978
1QPZ	-11.704	-10.395	1QP0	-10.165	-10.829	1QP7	-8.327	-8.595
1FJX	-12.070	-12.656	1J75	-10.165	-9.183	1JFS	-11.803	-9.749
1J5K	-7.529	-7.948	1PO6	-9.276	-9.960	1P51	-11.528	-11.533
1QZG	-8.614	-9.556	1OSB	-9.754	-10.591	1HVN	-7.227	-6.756
1BDH	-8.242	-8.219	1QP4	-10.906	-11.018	1QQB	-7.769	-8.286
1TW8	-12.192	-12.227	1QQA	-8.722	-8.317	1DH3	-12.070	-10.206
1JJ4	-11.991	-10.613	1FYM	-10.086	-9.461	1JH9	-11.859	-7.513
1JT0	-9.965	-10.345	1P78	-11.528	-11.583	1P71	-11.528	-11.213
1OMH	-9.754	-10.591	1S40	-12.983	-9.850	1U1L	-9.503	-8.936
1U1R	-9.053	-9.062	1U1N	-8.862	-9.658	1U1O	-9.855	-9.707
2BJC	-14.996	-9.751	1ZZI	-7.713	-8.013	2B0D	-8.242	-9.262
2GII	-12.783	-12.776	2GIE	-12.592	-12.521	2GIH	-12.252	-12.257
2ADY	-10.707	-10.172	2AC0	-10.364	-10.105	2AYB	-11.859	-11.788
2ERE	-10.256	-10.373	2GE5	-8.751	-8.892	2O6M	-10.751	-9.809
3D6Z	-8.204	-6.798	2VYE	-9.991	-9.824	3IGM	-8.590	-8.917
3HXQ	-12.572	-12.574	3EQT	-9.514	-9.441	3H15	-7.455	-8.787
2KAE	-11.039	-10.011	3MQ6	-12.572	-10.746	3JSP	-11.995	-11.719
3AAF	-8.994	-9.069	3N1L	-11.407	-11.236	3N1K	-11.236	-11.405
3R8F	-9.487	-10.296	2RRA	-7.940	-8.951	3QMI	-6.709	-6.751
2KXN	-7.700	-8.384	1U1P	-9.107	-9.258	1U1M	-8.901	-9.141
1U1K	-8.856	-9.163	1U1Q	-9.706	-9.535	2AOR	-8.242	-8.350
2AOQ	-7.438	-8.306	2I9K	-12.983	-11.709	2GIJ	-12.783	-12.774
2GIG	-12.252	-12.259	2CCZ	-9.543	-9.584	2AHI	-10.496	-10.172
2ERG	-10.364	-10.075	2AYG	-11.859	-11.878	2ES2	-8.843	-8.857
2ATA	-9.646	-10.318	2NP2	-9.897	-10.358	3D6Y	-6.799	-8.204
2VY1	-9.573	-9.601	3HXO	-12.572	-12.576	3GIB	-12.070	-9.609
3D2W	-9.355	-8.989	2KKF	-5.939	-8.127	3M9E	-9.388	-9.825
3JSO	-12.402	-11.298	3K3R	-11.966	-12.190	3N1I	-11.554	-11.383
3N1J	-11.386	-11.553	3KJP	-11.180	-9.073	3Q0B	-8.134	-9.216
3PIH	-11.890	-10.759	3QMH	-6.502	-6.837	3QMB	-7.438	-6.471
3U7F	-8.482	-8.392	3RN2	-9.476	-8.669	4ATK	-11.956	-11.746
2LTT	-10.628	-10.365	4HIO	-10.467	-10.124	4HIK	-10.388	-10.374
4A76	-9.855	-9.249	4HJ7	-11.209	-10.307	4HID	-8.273	-10.406

PDBID	Exp BA	Pred BA	PDBID	Exp BA	Pred BA	PDBID	Exp BA	Pred BA
4LJ0	-8.590	-9.679	4HT8	-9.471	-10.618	4GCK	-9.256	-9.238
4F2J	-10.364	-10.413	4GCT	-9.915	-9.734	4NI7	-13.223	-10.421
4CH1	-9.003	-9.759	4QJU	-8.768	-10.730	4ZBN	-13.194	-10.140
4R55	-7.876	-9.748	4S0N	-10.751	-9.187	4ZSF	-11.639	-10.971
4RKG	-6.258	-8.765	5A72	-9.916	-10.035	5DWA	-12.332	-10.702
5K83	-7.913	-7.139	5ITH	-10.256	-8.939	5W9S	-9.543	-7.754
5YI3	-8.534	-9.757	5XFP	-8.072	-8.756	5MEY	-9.265	-9.248
5MEZ	-9.001	-9.730	5W2M	-7.084	-7.220	5K17	-6.891	-9.173
6MG1	-10.276	-11.093	5VMV	-12.769	-9.678	6CNQ	-8.242	-8.450
6FQP	-9.229	-9.255	5WWF	-9.029	-9.019	6FQQ	-8.739	-9.723
5ZVB	-5.990	-5.836	5ZVA	-5.809	-6.133	5MPF	-9.605	-9.268
6G1L	-12.332	-11.436	6IIQ	-8.024	-8.421	6IIR	-7.570	-8.161
3ON0	-11.341	-10.307	4HQU	-14.586	-11.704	4HQX	-12.162	-13.473
4A75	-9.232	-9.772	3QSU	-10.511	-9.455	4HJ8	-10.440	-8.520
4HIM	-10.132	-10.460	4HJ5	-9.817	-10.383	4HP1	-7.028	-8.579
4J1J	-8.584	-10.562	4NM6	-8.140	-8.975	4GCL	-9.278	-9.652
3ZPL	-11.751	-10.172	3ZH2	-10.057	-11.072	4HT4	-11.039	-10.384
4LNQ	-8.011	-9.377	4LJR	-10.244	-9.756	4R56	-9.370	-6.727
4TMU	-12.030	-8.069	4R22	-10.819	-10.377	4Z3C	-7.661	-8.490
3WPC	-10.496	-11.373	3WPD	-11.619	-10.158	2N8A	-9.573	-10.047
5HRT	-12.114	-9.964	5T1J	-10.526	-10.033	5VC9	-9.265	-7.799
5HLG	-8.873	-10.626	5W9Q	-8.482	-7.439	6ASB	-7.940	-9.214
6ASD	-7.661	-8.398	5K07	-6.122	-8.960	5YI2	-9.738	-8.638
6MG3	-11.449	-10.346	6FWR	-8.873	-9.202	6CNP	-8.391	-8.260
5ZD4	-10.798	-9.287	5ZMO	-9.163	-9.864	6BWY	-6.251	-9.403
6CRM	-7.264	-12.078	6CC8	-7.181	-9.082	6BUX	-5.807	-7.718
6A2I	-8.701	-7.413	5ZKI	-8.015	-9.534	6KBS	-7.713	-9.784
5ZKL	-10.479	-10.217	5ZMD	-7.407	-9.116	6ON0	-9.605	-9.809
2A9X	-9.303	-10.954	3BX3	-9.874	-10.191	3IRW	-14.996	-10.855
3IWN	-12.270	-13.425	3K0J	-10.992	-13.428	3QGB	-11.528	-11.217
2XS2	-10.113	-7.906	3QGC	-10.982	-11.066	4GHA	-8.590	-9.489
3V6Y	-11.464	-11.555	2LUP	-6.090	-10.426	4M59	-9.531	-12.065
2MTV	-9.526	-7.928	4RCM	-6.350	-9.135	5EIM	-8.123	-8.359
5GXH	-7.661	-9.283	5KLA	-10.334	-11.348	5EN1	-8.942	-8.923
5F5H	-9.668	-9.273	5WZK	-9.265	-10.222	5HO4	-9.462	-9.199
5U9B	-9.388	-8.892	5WZJ	-10.751	-10.287	5TF6	-11.639	-10.691
5SZE	-10.459	-9.497	5WZG	-10.218	-10.339	5M8I	-5.736	-8.311

PDBID	Exp BA	Pred BA	PDBID	Exp BA	Pred BA	PDBID	Exp BA	Pred BA
5UDZ	-9.592	-9.344	5YTV	-8.043	-7.952	6FQ3	-8.015	-8.838
5YTX	-8.007	-7.982	5YKI	-12.030	-9.948	6DCL	-10.647	-8.916
6GD3	-5.191	-6.825	6G2K	-6.427	-6.511	6CMN	-11.727	-9.292
5YTS	-7.577	-7.671	5WWG	-9.077	-8.855	5YTT	-7.394	-7.775
6FQR	-6.073	-7.321	6GX6	-7.264	-6.222	5WWE	-8.550	-8.906
6GC5	-8.435	-7.224	6RT6	-6.755	-7.762	6NOF	-10.617	-10.431
6R7B	-10.558	-9.540	6NOC	-10.490	-10.469	6NOH	-10.421	-10.387
6A6J	-9.068	-8.487	6NOD	-10.280	-10.526	6G99	-6.176	-9.008
6RT7	-7.405	-7.314	6U9X	-10.086	-9.702	6NY5	-9.952	-10.192
6GBM	-5.556	-9.573	1EC6	-7.990	-9.004	1M8Y	-9.270	-12.497
1RPU	-13.300	-9.771	1UTD	-16.890	-9.030	2B6G	-10.600	-10.012
2ERR	-12.200	-9.110	2F8K	-10.300	-9.927	2G4B	-7.830	-8.468
2KFY	-8.840	-8.126	2KG0	-7.400	-8.128	2KG1	-7.450	-8.131
2KX5	-11.400	-9.967	2L41	-4.250	-7.744	2LA5	-11.500	-10.760
2LEB	-9.320	-8.734	2LEC	-9.440	-8.680	2M8D	-8.730	-8.680
2MJH	-9.670	-8.771	2MXY	-7.900	-6.914	2MZ1	-6.870	-7.871
2N82	-10.300	-10.363	2RU3	-8.520	-9.081	2XC7	-7.040	-8.859
2XFM	-8.240	-7.836	2XNR	-5.400	-7.462	2ZKO	-8.050	-10.219
3BSB	-10.200	-10.955	3BSX	-11.500	-10.696	3BX2	-9.970	-9.730
3K49	-12.050	-10.952	3K4E	-10.800	-11.859	3K5Q	-9.300	-9.072
3K5Y	-10.540	-9.511	3K5Z	-9.380	-9.682	3K61	-8.890	-9.531
3K62	-8.740	-9.253	3K64	-9.220	-8.886	3L25	-8.175	-9.260
3LQX	-12.220	-10.909	3MDG	-7.850	-8.917	3MOJ	-13.000	-10.957
3NCU	-10.300	-9.814	3NMR	-8.440	-7.299	3NNH	-6.190	-8.698
3O3I	-6.520	-7.070	3O6E	-7.070	-6.524	3Q0L	-12.300	-11.392
3Q0M	-12.500	-12.818	3Q0N	-10.500	-10.804	3Q0P	-12.800	-10.043
3Q0Q	-13.300	-12.542	3Q0R	-13.800	-12.954	3Q0S	-10.800	-11.713
3QG9	-10.600	-11.263	3U4M	-15.900	-10.085	3V71	-11.100	-10.371
3V74	-11.600	-11.382	3WBM	-9.980	-10.822	4CIO	-9.760	-9.002
4ED5	-9.080	-8.516	4ERD	-9.540	-10.329	4Jvh	-9.590	-9.484
4KJI	-8.940	-10.146	4LG2	-9.540	-8.843	4NL3	-7.380	-10.077
4O26	-8.200	-11.145	4OE1	-12.110	-9.541	4QI2	-9.440	-9.828
4QVC	-11.560	-9.994	4QVD	-10.120	-11.377	4R3I	-7.770	-6.765
4RCJ	-8.180	-8.440	4TUX	-10.400	-9.287	4U8T	-9.130	-7.841
4Z31	-8.790	-9.306	5DNO	-7.830	-8.538	5ELR	-6.250	-8.793
5V7C	-6.990	-9.070	5W1I	-12.790	-10.243	5WZH	-10.460	-10.308
6D12	-9.300	-10.271						